2024-01-2618

Effect of ambient pressure on ammonia sprays using a single hole injector

Li Shen and Felix C.P. Leach
Department of Engineering Science, University of Oxford, UK

Abstract

Ammonia has received attention as an alternative hydrogen carrier and a potential fuel for thermal propulsion systems with a lower carbon footprint. One strategy for high power density in ammonia applications will be direct injection of liquid ammonia. Understanding the evaporation and mixing processes associated with this is important for model development. Additionally, as a prior step for developing new injectors, it is of interest to understand how a conventional gasoline direct injection (GDI) injector would behave when used for liquid ammonia without any modifications. Pure anhydrous ammonia, in its liquid form, was injected from a single hole GDI injector at a fuel pressure of 150 bar into an optically accessible constant volume chamber filled with nitrogen for ammonia spray measurements. The chamber conditions spanned a wide range of pressures from 3 – 15 bar at an increment of 1 bar or 2 bar between the test points. These conditions lead to sprays which are both flash boiling and non-flash boiling as well as in a transition region. Spray morphology studies were performed based on high-speed backlit images recorded at 10 kFPS. Droplet size distributions for the bulk spray were simultaneously measured using a laser diffraction technique at the same sampling rate. The results show that at a higher ambient pressure, shorter spray penetration lengths and smaller spray spread widths are observed compared to those at lower pressures. While these macroscopic spray geometrical parameters change gradually at different ambient pressures, the droplet size distribution undergoes a slightly more abrupt transition across the saturation vapor pressure at chamber temperature. These results provide a fundamental dataset for liquid ammonia injection and could be used to validate against simulation data or to build surrogate models.

Introduction

The aim of achieving net zero by 2050 and limiting the global temperature increase within 1.5 °C requires inputs from all major energy sectors [1]. Maritime transport, despite being considered as one of the most efficient energy consumers, given its large share, still emits about 1076 million tonnes of CO_2 annually, equivalent to about 2.9% of total global greenhouse gas (GHG) emissions produced by human activities [2]. Ammonia (NH_3), a carbon free energy carrier, has significant potential to replace fossil fuels in this sector. As of 2021, over 230 million tonnes of ammonia are produced annually [3], predominantly by the Haber-Bosch process [4], mostly for conversion into fertilizer. As a consequence, a vast amount of mature infrastructure is already available for the production and the distribution of ammonia. Production of ammonia can also be 100% renewable, by producing the hydrogen feedstock from electrolysis powered by solar and wind, i.e., the so-called green ammonia [5]. Ammonia is an excellent hydrogen carrier and when liquefied (above 8.5 bar at 20 °C or below −33 °C at 1 bar [6, 7]), it contains 50% more hydrogen by volume than liquid hydrogen — the latter must be liquefied cryogenically (at around −250 °C depending on the pressure [6, 8]), requiring large amounts of energy. Outside of hydrocarbon (traditionally fossil) fuels, ammonia has among the highest energy densities of any alternative – its energy content per unit mass of stoichiometric mixture is comparable to conventional gasoline and diesel fuels [9]. Re-tooling existing production capabilities, and re-purposing existing knowledge would enable the green ammonia to be a zero-carbon fuel of choice for future transportation [10, 11] and a strong ally on the road towards net zero [12].

Prior to the energy release process, fuels need to be injected into thermal propulsion systems such as internal combustion engines and mixed with air. The evaporation (for liquid fuels) and mixing processes play an important role on the quality of energy release and the resulting emissions levels [13, 14]. While injecting ammonia as a gas would provide the best air-ammonia mixing locally, the global dispersion of the gas may be poorer than a liquid injection with a higher momentum to enhance the mixing. In addition, such gaseous injection, if injected in the inlet port (the so-called port fuel injection), would limit the amount of air that could be taken in to the cylinder, which negatively impacting the volumetric efficiency and power density [15]. Therefore, an ideal would be to inject liquid ammonia via direct injection (DI) to enable the maximum volumetric efficiency and ensure its complete vaporization as well as a constant fuel-air ratio throughout the chamber.

Recently, multiple studies have been conducted to promote the understanding of ammonia injections in both liquid and gaseous forms. Zhang et al. [15] used a Schlieren imaging system to visualize gaseous ammonia jets and compared against gaseous methane jets at the same conditions. It was found that when being injected in a gaseous form at a relatively low pressure (4 – 8 bar), ammonia gas jets showed a similar macroscopic characteristic (quantified by the tip penetration and the jet angle computed from the Schlieren images) to that of methane jets at low ambient pressures (1 – 4 bar). Pelé et al. [16] pioneered the experimental study on liquid ammonia injections from a multi-hole injector designed for gasoline direct injection (GDI). It was demonstrated that when the injection pressure is higher (120 bar) and when ammonia is injected in a liquid form, the ammonia sprays show a very different

behavior from liquid hydrocarbon fuels and biofuels such as gasoline and ethanol. While gasoline and ethanol sprays are similar in terms of geometry, ammonia sprays are "slimmer" — it has a smaller spray angle and longer penetration length compared to gasoline and ethanol sprays, and ambient pressures (or density) have a more profound effect on the geometry of ammonia sprays. Cheng et al. [17] also used the Schlieren technique to perform morphology studies on liquid ammonia sprays from a piezoelectric injector at an injection pressure up to 100 bar. Their study suggested that, owing to a lower viscosity and density, ammonia sprays tend to spread across a larger area compared to sprays from biofuels such as methanol and ethanol, and ammonia sprays evaporate much faster and have a more rapid mixing process with air. Fang et al. [18] examined liquid ammonia sprays from a diesel injector at high injection pressures (500, 750 and 1000 bar) and a wide range of ambient pressures (1 – 40 bar) using the backlit imaging technique, and found that there is a sudden drop on the average penetration speed of the spray tip when the ambient pressure was reduced to lower than the saturation pressure of ammonia.

However, experimental studies on ammonia injections are still limited [19]. The above-mentioned works show that ammonia behaves very differently with the extensively studied traditional fuels when being sprayed into similar ambient conditions, and the spray characteristics vary drastically under different ambient pressures. This calls for the necessity of performing an ammonia spray morphology study with a more dense selection of test points. Additionally, most of previous work has focused on macroscopic ammonia spray geometrical parameters, for instance penetration length and spray angle, and there is even more limited measurement taken on microscopic parameters such as droplet sizes, one of the key parameters when evaluating the quality of atomization from an injector. Liu et al. [20] recently used a Particle Droplet Image Analysis (PDIA) system to measure the droplet sizes of ammonia sprays at a relatively low injection pressure of 10 bar, and reported that the variation of ambient pressure also has a notable effect on the droplet sizes within the plume.

In this paper, a single-hole GDI injector, operated at a relatively high injection pressure (150 bar), was used for liquid ammonia injections, with the aim of examining the effect of ambient pressure on macroscopic and microscopic behaviors on ammonia sprays, and for testing how a conventional injector would behave when ammonia is used as the injected fluid under its typical operation pressure. To examine how ammonia sprays would behave under different ambient pressures in a more detail, the test points (chamber pressures) were selected to be closer to each other (at 1 bar increment) around the saturation pressure of ammonia at the room temperature, and these test points cover both the flash-boiling [19] and the non-flash boiling conditions, as well as a transition region between them. The macroscopic characteristics of ammonia sprays were captured by the backlit imaging technique at a frame rate of 10 kFPS, and spray morphology studies were performed after processing the raw backlit images following the SAE J2715 standard [21, 22]. On a microscopic level, droplet size distribution within the spray plumes for each backlit image was simultaneously measured using the laser diffraction technique. The experiments provide a fundamental spray breakup and mixing data set for ammonia-air mixtures, and the data set may be used for model validation.

Experimental Setup

Test Rig

Ammonia spray measurements were performed in an optically accessible constant volume chamber filled with nitrogen gas at various ambient pressures. Figure 1 illustrates a schematic of the chamber and the experimental setup in two view orientations. The top subplot provides a view from the top of the setup, and the bottom subplot provides a front view (which is also the view for the high speed camera to be introduced in the next paragraph). An injector was mounted along the symmetrical axis of the chamber and with its own axis pointing downwards, and the injected fluid (liquid anhydrous ammonia) was fed from the top. The liquid ammonia was pressurized by a nitrogen-driven pump (Heypac GX40 series) placed near the chamber from a lower pressure supply stored outdoors. A dedicated ammonia manifold and delivery system (see [23] for details) was built as per the safety regulations [24, 25, 26, 27]. The injection current profile was preset by an injector driver provided by the manufacturer of the injector, and the injection duration was controlled by the width of a TTL pulse sent to the injector driver from a pulse/delay generator (Berkeley Nucleonics Corporation BNC 525). The injection (Kistler Type 4007D) and chamber (GEMS 3100 series) pressures were respectively measured by pressure sensors, and their readings were recorded by a high-speed data acquisition card (National Instruments USB-6211).

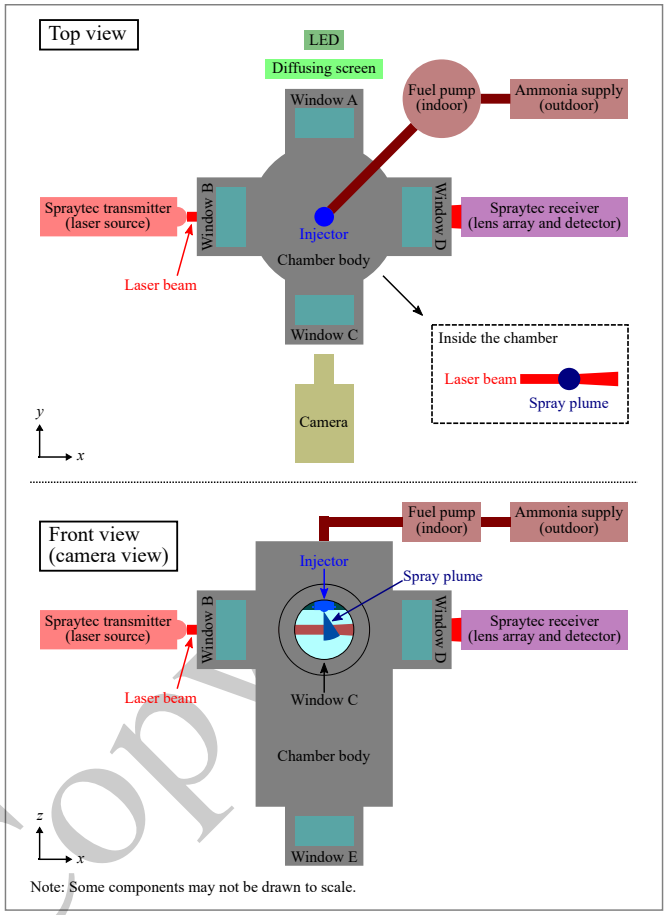

Figure 1: A schematic of the chamber and the experimental setup in two view orientations. The top subplot provides a view from the top of the setup, and the bottom subplot provides a front view (also the camera view). The optical access is provided by the quartz windows, colored in cyan and labeled from Window A to Window E. Each window has a 80 mm viewable diameter.

The optical access of the chamber is provided by five quartz windows – two pairs on the side with an orthogonal layout (denote Windows A-D in Figure 1) and the fifth one at the bottom (denote Window E, not used in this experiment). Each window has a viewable diameter of 80 mm. A diffusing screen was placed in front of an LED light source which offered a uniform white-light illumination to the chamber from one of

the side windows (Window A) for the backlit imaging tests. A high-speed camera (Photron FASTCAM-1024PCI model 100K) was aligned at the same height of the window on the opposite side (Window C) to record the spray images.

The optical access provided by the other pair of side windows, i.e., Window B and Window D in Figure 1, were used for measuring the droplet size with a Malvern Spraytec device using the laser diffraction technique. The Spraytec device is composed of two parts [28], namely the transmitter and the receiver. The transmitter emitted a collimated beam of 10 mm in diameter from a helium-neon laser at a wavelength of 632.8 µm, and the beam entered the chamber through Window B. As illustrated by an enlarged (and exaggerated for a better visualization) view in Figure 1, when the beam hit the spray plume, the light was scattered by the droplets inside the plume. Different diffraction patterns were then generated depending on the size of the droplets, among which the smaller droplets tend to scatter light at a larger angle. The scattered light exited the chamber via Window D on the opposite side, and they were collected by a lens assembly and then by the photodiode detector elements in the receiver. The photodiode detectors are arranged as circles (more precisely, arcs) at different radius but sharing the same center with the laser beam from the transmitter, so that the scattered light at various angles can be collected by different detectors. The portion of laser energy collected by each detector therefore indicates the relative frequency of droplets at a certain range of sizes. This correlation was later processed by the Spraytec software (version 4.00) to generate a droplet size distribution chart. The 300 mm lens assembly was chosen to enable a measurement of droplet size ranging from 0.1 – 900 µm. The volume-based droplet size distributions are reported in this manuscript instead of number-based ones, since this result interpretation method is recommended when using the laser diffraction technique [28]. For each droplet size distribution, the Sauter Mean Diameter (SMD) [29, 30, 31] was also computed to quantify the overall size of the droplets. Besides the scattered light, there was a portion of light from the transmitter passed through the test region while remained un-scattered, and an aligned detector on the receiver side measured this part of laser energy and reported its value relative to the total energy emitted from the laser as "the relative laser energy transmission".

It should be noted that the laser diffraction technique is not equivalent to a droplet counting process at a single point (known as a temporal measurement, for example the Phase Doppler Anemometry (PDA) technique [32]). Instead, it provides a spatial measurement on the bulk behavior of the spray at a given time [33], and in other words, all the droplets within the measurement region (defined as the intersection between the laser beam and the plume) at the time when the measurement was taken would contribute to the final droplet size distribution.

Test Conditions

The injector used in this set of tests is a single hole Bosch injector, and, by design, it has a 20° spray (centerline) angle with respect to the injector axis and a hollow cone plume pattern. The nominal nozzle diameter is about 550 µm, which was measured using the X-ray computed tomography (XCT) technique in a commercial device (North Star Imaging ImagiX CT Scanner). While the injector was designed for gasoline direct injection, in this experiment, the injected fluid was liquid anhydrous ammonia at 150 bar. The injector was activated by the injector driver (Bosch ES-HDEV-1) which received a TTL pulse from the pulse/delay generator at a fixed duration of 2 ms to perform a series of 10 shots at 1 Hz (i.e., one shot at every second). Before each test, the chamber was charged with nitrogen gas to the desired ambient (i.e., chamber) pressures, varying from 3 – 15 bar at a 1 bar (below 11 bar) or 2 bar increments (above 11 bar) — there are 11 test points in total. The chamber was vented and purged with nitrogen gas between test points. Both the injection line and the chamber were kept at room temperature (20 °C) during the tests. As the saturation pressure of ammonia is 8.5 bar at this temperature [6, 7], the selected test points included both non-flash boiling cases at higher ambient pressures and flash boiling cases at lower ambient pressures. The small increment also allowed the examination of the transition region between these cases. Figure 2 illustrates a comparison of the test points in the present work and in recent literature [15, 16, 17, 18, 20] for ammonia spray measurements conducted near room temperature. Note that different injectors are used in these works, and for a clearer visualization, the injection pressure is plotted in a log scale.

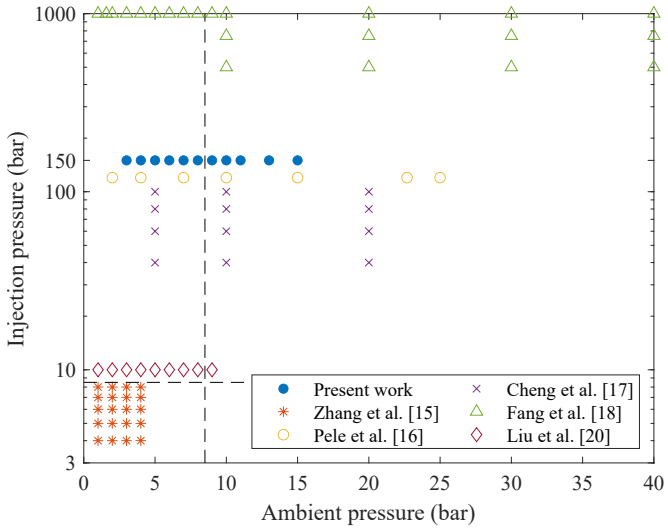

Figure 2: Test points for ammonia spray measurements at room temperature (near 20 °C) in the present work and in recent literature [15, 16, 17, 18, 20]. The black dashed lines mark the saturation vapor pressure of ammonia (8.5 bar at 20 °C [6, 7]). Note that different injectors are used in these works.

Synchronized with the injector by the pulse/delay generator, the camera recorded backlit images for each shot of ammonia sprays through Window C at 10 kFPS (and 0.1 ms shutter speed) from 0.5 ms before the start of injection to 9 ms after the start of injection (aSOI). These 8-bit monochrome images are 256 pixels in width and 272 pixels in height, and the resulting resolution is 0.25 mm per pixel. Raw images were processed using an in-house algorithm to be discussed in the next section for spray morphology studies. Figure 3(a) provides an example of the raw images recorded at 1.3 ms aSOI for the 10 bar ambient pressure test point. As the LED light source required a finite time period to reach a stable output, it was triggered 2 ms before the camera so that the luminosity stayed almost the same for all the images in each shot.

In our experiment, the center of the beam was aligned with the center of the spray plume along the radial direction (see the top view in Figure 1) and at 26.5 mm below the injector tip. The red shaded areas superposed on the backlit image in Figure 3(a) illustrate the location of the beam, and note that while the beam did pass the plume (darker pixels), the darker pixels from $x = 0$ to $x = 20$ mm were not covered by the red shaded area for a better visualization of the plume. The effective measured volume was a cylindrical region of 10 mm in diameter (beam diameter, ranging from $z = -21.5$ to $z = -31.5$ mm) and about 20 mm in length (path length of the plume at this height along the beam direction, i.e., the x-axis direction). The Spraytec device was triggered by the pulse/delay generator at the same time as the high-speed camera, and at a 10 kHz sampling rate, it measured the volume-based droplet size distribution simultaneously with the backlit images, i.e., one droplet size distribution chart for each backlit image. The above-mentioned key parameters for the experiment are summarized in Table 1.

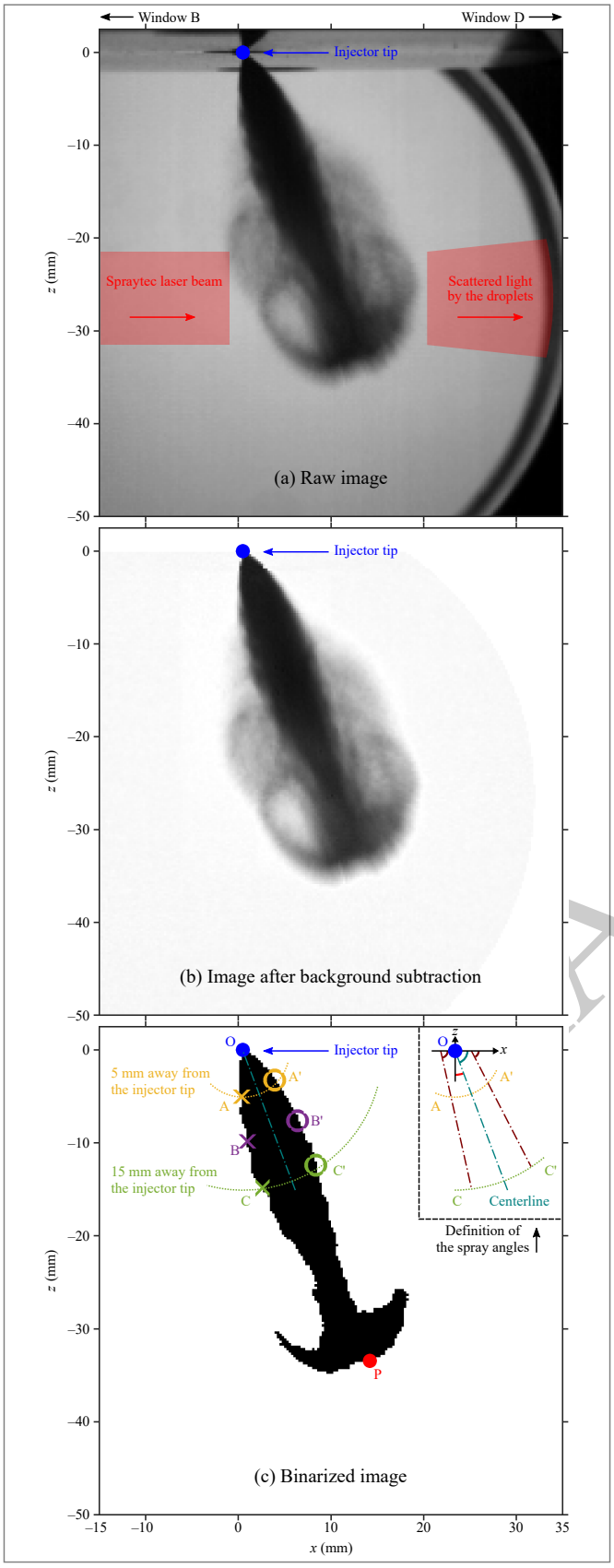

Figure 3: Steps for the spray image processing. The colored markers and lines are superposed on monochrome images for illustration of the algorithm.

Table 1: Parameters for the experiment.

Parameter	Value
Chamber dimension	160 mm (internal diameter) 281.5 mm (effective height) 7.2 L (internal volume)*
Window dimension	80 mm (viewable diameter)
Ambient gas in the chamber	Nitrogen gas, oxygen free
Ambient pressure	3, 4, . . . , 10, 11, 13, 15 bar†
Ambient temperature	20 °C
Injector model and type	Bosch single hole, hollow cone
Injector nozzle diameter	550 µm
Injected fluid (sat. pressure at 20 °C)	Liquid anhydrous ammonia (8.5 bar [6, 7])
Injection pressure	150 bar
Injection temperature	20 °C
Injection duration	2 ms
Injection frequency	1 Hz
Camera frame rate	10 000 FPS
Camera shutter speed	0.1 ms
Image resolution	0.25 mm per pixel
Spraytec sampling rate	10 000 Hz
Spraytec beam diameter	10 mm

* The additional volume is held by the window housings.
† All pressure values in this manuscript are reported in absolute pressure units.

Image Processing and Macroscopic Parameters

Raw images such as Figure 3(a) need to be processed before computing macroscopic parameters including the penetration lengths, the spray centerline angle and the spray spread widths for spray morphology studies. The images recorded before the start of each injection were used as a background since they were free from droplets. Given that the LED light source provided an almost constant illumination during each shot, the averaged background images were subtracted from the raw images, and this procedure effectively removed the stationary chamber features that are not relevant to the spray (such as the injector mount and the housings for the quartz windows). In the resulting background subtracted images (Figure 3(b)), the plume can be qualitatively separated into two parts – a darker region of a dense plume body penetrated from the injector tip to the front edge, and a slightly brighter region composed by a mist of discrete droplets surrounded the plume body.

The spray macroscopic parameters were computed from a modified algorithm based on the SAE standard J2715 [21, 22]. While in the original algorithm the spray backlit images were directly used for computing the parameters, it was found that the mist of discrete droplets in Figure 3(b) would skew the results due to the nature of the algorithm to be introduced in the following paragraphs. Therefore, an additional procedure was added — a locally adaptive method (known as the Bradley's method [34]) was applied to binarize the background subtracted images to obtain images like Figure 3(c). This process isolated the plume body in the foreground from the brighter background, and since the local mean intensity was used as the binarization threshold, the blurred outer plume edges composed by the mist of discrete droplets were also removed.

For each binarized image as exemplified in Figure 3(c), the spray macroscopic parameters were calculated using the following procedure. An arc (marked by a dotted yellow line) at a fixed radius of 5 mm away from the injector tip (blue dot, or Point O) intersects with the plume body (black pixels) at two points – the left-edge intersect Point A (yellow cross) and the right-edge intersect Point A' (yellow circle). The same procedure was repeated at 15 mm away from the injector tip (dotted green line) to obtain Point C (green cross) and Point C' (green circle). In an illustrative plot at the top-right corner of Figure 3(c), imaginary lines A-C and A'-C' can thus be drawn (brown dash dotted lines), and by averaging their angles with respect to the positive x-axis (marked by brown arcs), one can obtain the spray centerline (teal dash dotted line) which passes through the injector tip. Since the injector axis pointed downwards in our setup and there was only one plume from the single-hole injector, without loss of generality, the "spray centerline angle" (marked by a red arc) was defined by a positive angle between the spray centerline and the negative z-axis. The value is 19.4° for the example image in Figure 3(c).

Additionally, the lengths of line segments A-A' and C-C' in Figure 3(c) suggest how wide the plume body has spread at some fixed distance away from the injector tip. Therefore, the so-called "spray spread width" could be obtained as a function of distances away from the injector tip by these lengths – 4.1 mm for A-A' (5 mm away) and 6.7 mm for C-C' (15 mm away). Analogously, the spray spread width at any other distance could also be computed — for instance at 10 mm, the plume edges are Points B and B' (purple cross and circle, dotted arc not shown for brevity), and hence the spray spread width at 10 mm away from the injector tip is the length of line segment B-B' (5.5 mm).

Among all the darker pixels which indicate the existence of the plume body in Figure 3(c), Point P (red dot) is the furthest point away from the injector tip (Point O), and hence the distance O-P, which reads 36.3 mm in this example image, defined the "maximum penetration length". It should be noted that Point P does not necessarily lie on the spray centerline, as the shape of the front edge of spray is prone to be changed by its interaction with the ambient gases.

Visual inspections of the background subtracted images suggested that (Figure 3(b)), at a fixed time after the start of injection, the plume body stayed roughly at the same location among different shots for a specific test point (i.e., ambient pressure). For the droplet mist around the outer edge of the plume, however, due to the frequent interaction (mixing and re-circulation) with the surrounding gases, its shape may deform differently from shot to shot even at the same test point. If the algorithm were applied to the background subtracted images directly in its original form, without the removal of the mist of discrete droplets whose shape changes randomly, the locations of the key intersections such as Point C and Point C' would vary significantly from shot to shot, resulting a huge variation in the derived parameters such as the centerline angle and the spread widths. This would further conceal the focus of this paper when comparing these parameters among different test points (i.e., at different ambient pressures), as such a random mixing process may occur at any time of any shot regardless of the ambient pressure conditions. Therefore, the algorithm was applied to the binarized images after removing the droplet mist in this paper.

Results of Spray Morphology Studies

Observations from Single-Shot Spray Images

Figure 4 shows a series of background subtracted images, from which each subplot was taken at different times after the start of injection (rows, where the subplot labels are marked in a red font color for clarity) and/or under various ambient pressure conditions (columns, subplot labels marked in blue). At 0.6 ms aSOI (the first row, Figure 4(a1)-(a4)), the spray has penetrated for over 15 mm under all the tested ambient conditions, but the size of the plume for each condition is different — at 5 bar (Figure 4(a4)), due to a lower ambient density and thus a lower resistance for the spray to penetrate, its plume covers about 69% more line-of-sight area than the 13 bar point (Figure 4(a1)) with a wider spread angle and a longer penetration length. In addition to the cone-shaped plume body, there is a pilot stream, a design feature of this hollow cone injector, penetrating at a longer distance away from the nozzle (marked by a purple dotted circle in each subplot).

As the plume continued penetrating, at 1.0 ms aSOI (the second row, Figure 4(b1)–(b4)), the pilot stream slowed down and under higher ambient pressures (13 bar for Figure 4(b1) and 9 bar for Figure 4(b2)), it was caught by the main plume body and was no longer visible in the line-of-sight backlit images. On the other hand, the lower resistance provided by the lower ambient pressure (and hence lower density) conditions enabled the pilot stream at 5 bar (Figure 4(b4)) to travel further, and it was not until at 1.4 ms aSOI (Figure 4(c4)) that the pilot stream was finally covered by the main plume body in the image. Also, in Figure 4(b1)–(b4), the front edge of the plumes showed a flat or even concave shape, revealing a stronger resistance from the ambient gases at regions where the axial speeds were higher such as near the centerline of the plume. Due to the shearing flow generated as the high-speed spray entering the quiescent environment, the wake of the plume circulates around the plume body (darker pixels) from both sides.

Meanwhile, a plume necking phenomenon (marked by a dotted lime green circle) was observed in Figure 4(b1) — the width of the plume body maximized at about 15 mm away from the injector tip, and the plume body became narrower downstream when intruded by the shearing vortices. Consequently, the ammonia droplets in those regions might undergo a faster breakup and evaporation process thanks to the increased mixing with surrounding gases induced by the vortices, and this leads to a brighter region as seen in the images. The plume necking phenomenon was not yet obvious at 1.0 ms aSOI for the lower ambient pressure conditions (Figure 4(b2)–(b4)). At 1.4 ms aSOI (the third row, Figure 4(c1)–(c4)), however, this phenomenon was seen in all the tested conditions as the plume penetrated at a longer distance, and the supply from the nozzle was not sufficiently strong to compensate the rapid breakup and evaporation of droplets in those regions.

At the end of the 2-ms injection, i.e., at 2.0 ms aSOI (the fourth row, Figure 4(d1)–(d4)), the front edge of the plume has exceeded the effective field of view (FOV, about 53 mm away from the injector tip) in lower ambient pressure conditions (Figure 4(d2)–(d4)), while at a higher ambient pressure (Figure 4(d1)), the plume has not yet reached the edge of the window. This is again due to lower resistances in lower pressures enabling the plume to penetrate further away from the nozzle.

Once the injection has stopped, the remaining plume has no supply from the nozzle and will gradually evaporate in the chamber. At 1.5 ms after the end of the 2-ms injection, i.e., at 3.5 ms aSOI (the fifth row, Figure 4(e1)–(e4)), there were still quite a lot of droplets remaining in the FOV for all the test points. While these images seem to be similar, differences can still be observed. Near the injector tip (marked by a dotted brown circle), the plume has not yet left this region at the 13 bar test condition (Figure 4(e1)) due to the strong resistance from the denser ambient gases. On the other hand, at the 5 bar point (Figure 4(e4)) this region was almost free from droplets, since there was less resistance to prevent the droplets from traveling further. Although it is not shown here for brevity, all the droplets have evaporated before the next shot (1000 ms after the start of the previous one). To facilitate the discussion on droplet sizes in a later section, the red dashed lines in each subplot of Figure 4 indicate the boundary of the Spraytec laser beam, i.e., the cylindrical sampling area of the laser diffraction technique.

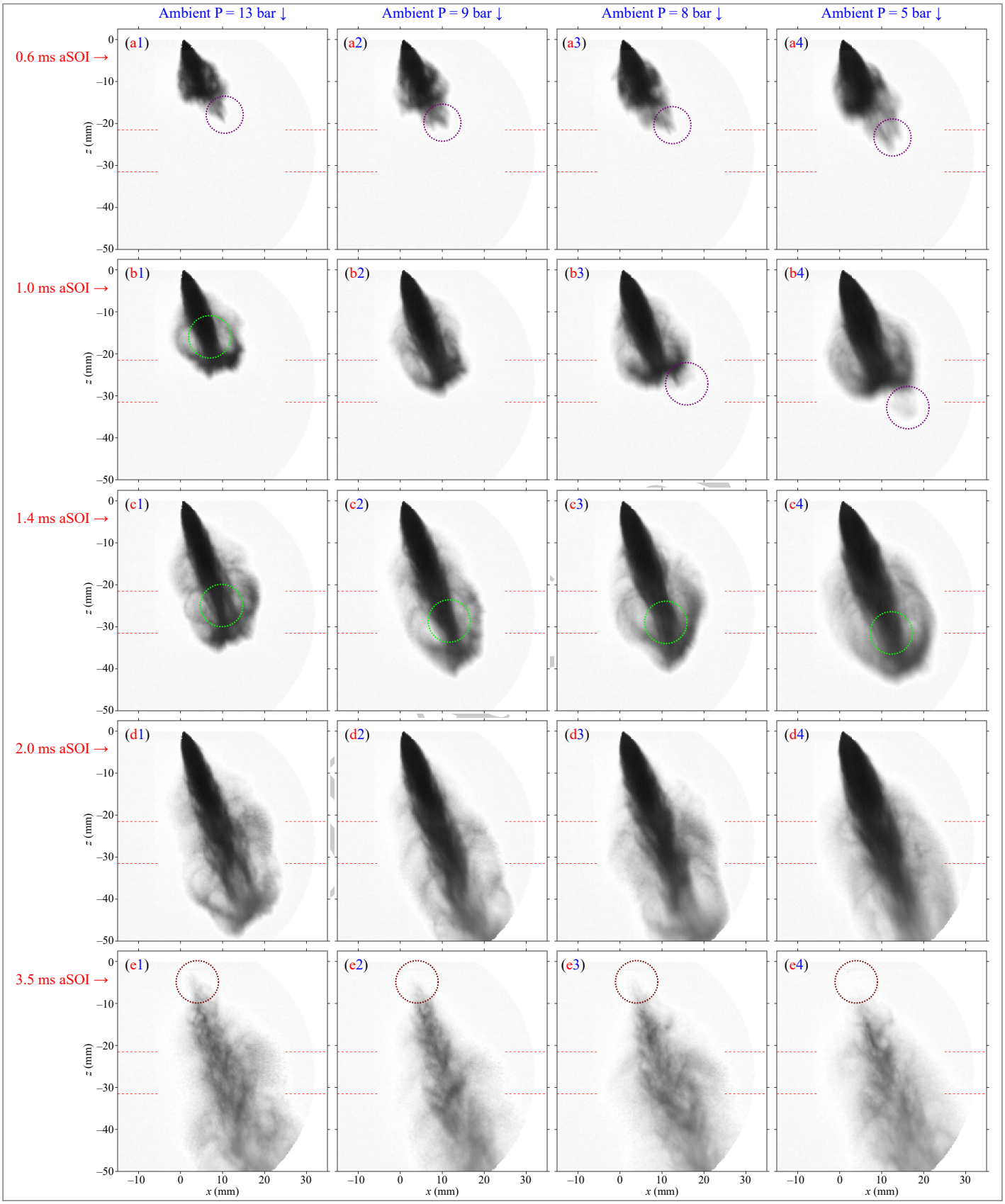

Figure 4: Ammonia spray images taken at different timings (rows) and ambient pressure conditions (columns). The colored circles superposed on the monochrome images mark the key features discussed in the paper. The dashed red lines indicate the boundary of the Spraytec laser beam (i.e., the laser diffraction sampling area).

Spray Macroscopic Parameters

The observations made from the spray images provided a qualitative view of the ammonia sprays under the tested conditions. However, it would also be important to compute some quantitative parameters to extract the information from numerous images taken during the tests. With the help of the spray macroscopic parameters defined in the Image Processing section, the spray morphology study can be performed across different test points to further examine how the shape of the spray transit from non-flash boiling cases (when ambient pressures are higher than the global saturation pressure) to flash-boiling cases (lower ambient pressures). Figure 5(a) shows the maximum spray penetration length as a function of time in the unit of ms aSOI from the 15 bar to 5 bar ambient pressure test points. For all statistical values reported here in Figure 5 and in later figures in this manuscript, the filled markers (for test points with ambient pressures higher than the global saturation pressure) and the hollow markers (for test points with ambient pressures lower than the global saturation pressure) refer to the median value (i.e., the second quartile) of the 10 repeated shots at each test point, while the lower and upper bounds of the error bars are the first and the third quartiles, respectively.

Intuitively, at each chamber pressure (say, at 5 bar, the brown markers in Figure 5(a)), the spray penetrated for a longer distance at a later timing, until the front edge of the plume exceeded the FOV at 53 mm (at which point the calculation ceases). There was a rapid increase before 0.6 ms aSOI, and after checking the raw images, this was due to the pilot stream discussed in the previous section leaving the nozzle at a higher speed compared to the main plume body. As the pilot stream lost its momentum owing to the resistance from the ambient gases, it was slowly caught up by the main plume which has a continuous supply from the nozzle (illustrated before in Figure 4), and hence the maximum penetration length remained almost unchanged at around 0.8 ms aSOI for the test points below 13 bar ambient pressure, until after 1.0 ms aSOI the values started to increase again as the main plume continue penetrating further away from the injector tip. On the other hand, such a phenomenon was less obvious at the 15 bar chamber pressure (blue markers), since its pilot stream slowed down much more rapidly in the denser environment and hence the pilot stream did not deviate from the main plume body at the very beginning of the injection.

Viewing from another perspective in Figure 5(b), when the maximum penetration lengths are plotted in an equally spaced timing as a function of ambient pressures, it is clearer that the rate of change for the maximum penetration length varies at different timings. The values escalated by about 18 mm from 0.3 ms aSOI (brown markers) to 0.6 ms aSOI (green markers), while the rise from 0.6 ms aSOI to 0.9 ms aSOI (purple markers) was only less than 5 mm for most of the test points during which the pilot stream slowed down and was picked up by the main plume body. The main plume body then continued penetrating afterwards and was gradually decelerated by the stationary ambient gases downstream. Once again due to the lower resistance, the spray penetrated for a longer distance at lower ambient pressures at the same timing. A smooth transition from the non-flash boiling to the flash-boiling conditions was observed across the global saturation pressure (8.5 bar), and there was no clear boundary between these two categories.

Figure 6 shows the spray centerline angles (with respect to the injector axis as defined in the Image Processing section) as a function of time. While there are some variations, for all the available data points, the spray centerline angle fell within ±2.5° of the designed value (20°). This reflects that, for the tested single-hole injector, varying ambient pressures and/or changing the working fluid from iso-octane to ammonia has a minimal effect on the overall direction of the spray. Note that in this manuscript the spray angles were only computed from the images taken after 0.9 ms aSOI since the algorithm introduced in the

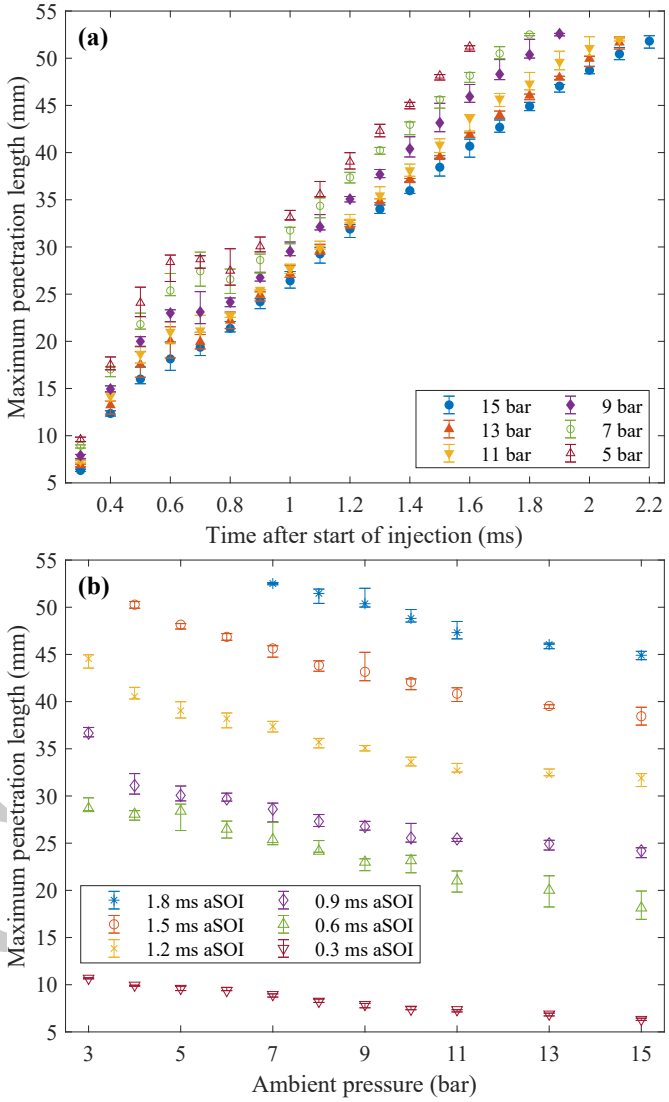

Figure 5: Maximum spray penetration lengths (a) as a function of time after the start of injection under different ambient pressures and (b) as a function of ambient pressures under different timings. The filled/hollow markers refer to the median value (i.e., the second quartile) of the 10 repeated shots at each test point, while the lower and upper bounds of the error bars are the first and the third quartiles, respectively. This approach applies to all of the figures in this manuscript.

Image Processing section requires the spray to penetrate for a sufficiently long distance (set to be over 25 mm) away from the injector tip so that to provide a robust evaluation of these parameters.

The overall shape of the plume body can be examined by the spread widths at various distances away from the injector tip as shown in Figure 7. At 1.4 ms aSOI, as discussed in the previous section and illustrated before by the images in Figure 4(c1)–(c4), the pilot stream has been covered by the main plume body at all test conditions, and the so-called plume necking phenomenon was observed — in Figure 7 for the 5 bar chamber pressure (brown hollow markers), the spray spread width firstly increased from 4.4 mm (at 5 mm away) to the maximum value at 8.1 mm (at 16 mm away), and as the spray penetrated and moved further away from the injector tip, there was a sudden drop (down to 4.7 mm) in its width when the spray was more than 16 mm away from

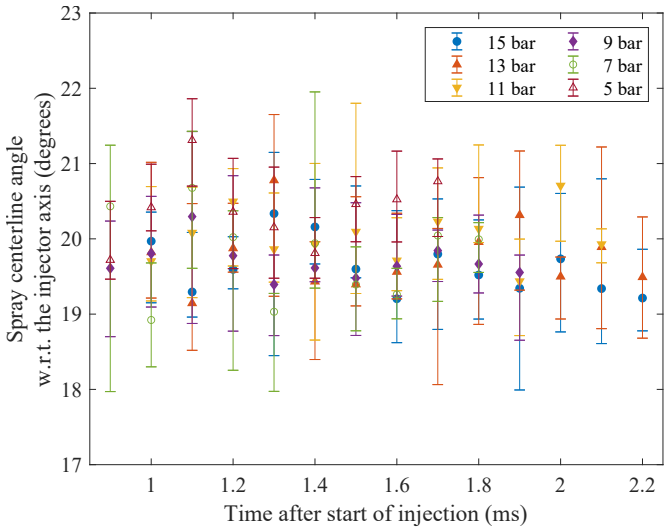

Figure 6: Spray centerline angles as a function of time after the start of injection under different ambient pressures.

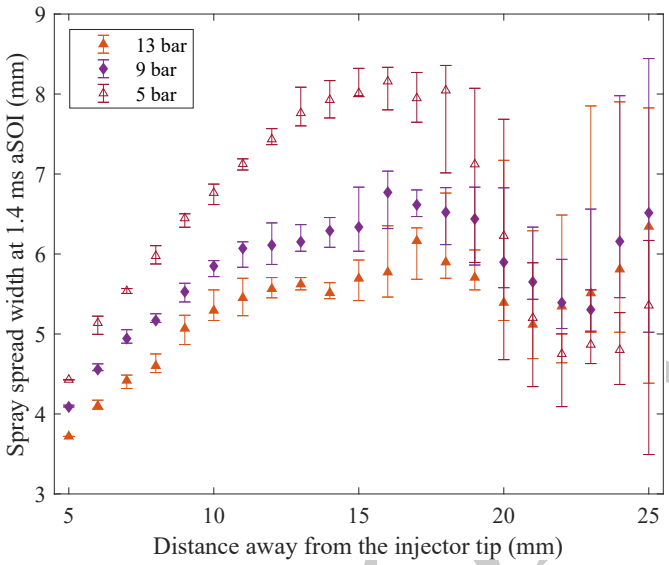

Figure 7: Spray spread width as a function of distance away from the injector tip at 1.4 ms aSOI under different ambient pressures.

the injector tip. In this region, the error bars also spanned a wider range, showing that the shot-to-shot variation was more significant further downstream of the plume (when the distances are larger) and the exact location at which the plume neck occurred may fluctuate in different shots. Such a phenomenon also existed at higher ambient pressures (at 9 bar and 13 bar in Figure 7), but their widths at the plume neck decreased to a slightly smaller extent, potentially due to a slower evaporation process under these non-flash boiling conditions.

Results of Spray Droplet Size Analysis

The spray morphology studies based on backlit images discussed in the previous section offered macroscopic views on how the spray plume changed at different ambient pressures. The laser diffraction method, on the other hand, enabled an insight of how the droplets evolved within the plume in terms of their sizes. As illustrated previously in

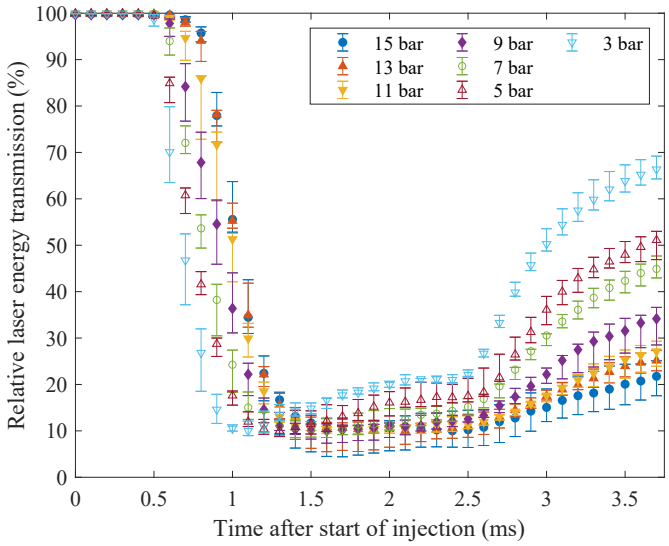

Figure 8: Relative transmission of the laser diffraction method (the amount of un-scattered light normalized by the total laser energy) as a function of time after the start of injection under different ambient pressures.

Figure 3(a), droplet size distributions were measured in a cylindrical region at 21.5 – 31.5 mm below the injector tip, and therefore it would take some time for the spray plume to penetrate from the injector tip to the measurement region. The relative laser energy transmission (i.e., the amount of un-scattered light normalized by the total laser energy, measured by an aligned detector introduced the Experimental Setup section) provided an estimate of whether the majority of the plume had entered the test region and helped to determine the sampling window (i.e., timings of interest) for the droplet size measurement, and the values are reported in Figure 8 as a function of time under different ambient pressures.

For all test points, the relative transmission values remained higher than 99% before 0.5 ms aSOI when the spray plume had just left the nozzle and there were no droplets within the measurement region. As the spray plume continued penetrating downwards, depending on the ambient pressures, it took 0.6 ms (at 3 bar, light blue hollow markers) to 0.9 ms (at 15 bar, blue filled markers) for the first visible drop in transmission to occur. Note that the measurement region was fixed in location, this timing differences also suggested that ambient pressures (and hence the density) have a profound effect on the penetration length of the spray plume, as it took a longer time for the spray to reach the measurement region when the ambient gases were denser and the spray needed to overcome more resistances at higher pressures.

Within the next 0.3 ms, for all conditions, the transmission values were reduced by over 80% as the main plume body rapidly entered the measurement region and the droplets started scattering the laser beam. The relative laser energy transmission remained below 25%, until after about 2.6 ms aSOI (or 0.6 ms after the 2-ms injection), as the supply from the injector had stopped and the evaporation was taking over, the droplets within the measurement region diminished and the transmission values gradually increased. Notably, under flash-boiling conditions (lower ambient pressures), the rate of increase in the transmission, which at this timing could be regarded as an indication of the rate of evaporation, was much higher than the non-flash boiling conditions (higher ambient pressures), especially for the 3 bar test point.

As the laser diffraction technique relies on the presence of a sufficiently large number of droplets in the measurement region, in the following

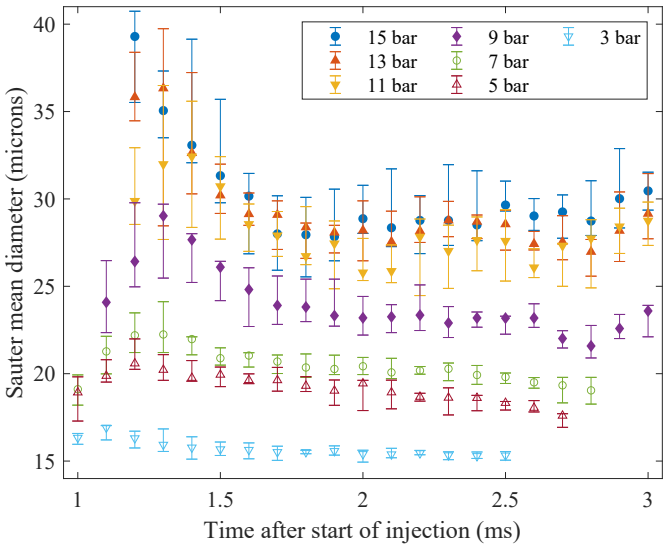

Figure 9: Sauter mean diameter as a function of time after the start of injection under different ambient pressures.

analyses, the sampling window for the droplet size measurements are set to be the time at which the relative laser energy transmission was below 25% for each test point. The choice of this threshold matches with the observation made from the raw images. For instance, for the 5 bar test point, the relative laser energy transmission (brown hollow markers in Figure 8) first dropped below 25% at 1.0 ms aSOI, and the raw image in Figure 4(b4) suggested that the main plume body had entered the Spraytec measurement region (between the two red dashed lines) at this timing. For each test condition, droplet size data points beyond the sampling window (i.e., when the transmission value was too high and there were not enough droplets in the measurement region) were discarded from the later plots (Figures 9 – 12).

The Sauter mean diameter (SMD), defined in [29, 30, 31] and computed by the Spraytec software, provides an estimate on the overall size of the droplets within the measurement region. As shown in Figure 9, the values of SMD reduced as the ambient pressures decreased from about 30 µm at 15 bar (blue filled markers) to about 16 µm at 3 bar (light blue hollow markers), as a result of a stronger evaporation for the lower pressure (flash-boiling) cases. For each of the three flash-boiling conditions (hollow markers) in Figure 9, despite a gradual drift towards smaller values at later timings potentially due to the evaporation of larger droplets to smaller ones, the SMD showed a minimal variation with respect to time. At the 5 bar test point (brown hollow markers), for instance, the values fell within a narrow range of 17.6 – 20.6 µm for all available data points from 1.0 – 2.7 ms aSOI. There was, however, a more notable decrease in the SMD values for the non-flash boiling conditions during an early stage (from 1.2 – 1.6 ms aSOI), until the values finally stabilized after 1.7 ms aSOI. When the ambient pressure was at 13 bar (orange filled markers in Figure 9), the SMD dropped by almost 25% from 36.3 µm to 27.5 µm within 0.9 ms. This may be a combined result of plume motion and droplet breakup within the measurement region — larger droplets tended to carry more momentum to move further downstream and therefore entered the measurement region sooner than the smaller ones to cause a larger SMD at earlier timings, and within the measurement region these larger droplets were also prone to breakup into smaller ones in the denser environment, resulting in a decrease in the SMD at a later timing.

Comparing the SMD values among different chamber pressures, at each measured timing, the values for the three flash-boiling conditions (3, 5 and 7 bar) were quite distinct — their error bars in Figure 9 were separated from each other after 1.2 ms aSOI. This reveals that, under these lower pressures, the change in global ambient pressure has a profound effect on the extent of flash boiling and hence the resulting droplet sizes. On the other hand, while the pressure difference between neighboring test points plotted in Figure 9 was the same (2 bar) as the flash-boiling conditions, for the non-flash boiling conditions (11, 13 and 15 bar), their SMD values were much closer to each other; and despite the general reducing trend from higher ambient pressures to lower ones, there were overlays for the error bars among these test points. In other words, the change of ambient pressure does not have a strong effect on the droplet sizes under non-flash boiling conditions. Interestingly, at the 9 bar test point (purple filled markers), although the global chamber pressure was higher than the saturation pressure (8.5 bar), its SMD values deviate from the ones for the other non-flash boiling cases, and the values were almost equally distanced away from the 11 bar test point (yellow filled markers) and the 7 bar test point (green hollow markers) at each measured timing. This indicated that at the 9 bar test point a partial flash boiling phenomenon likely occurred within the plume — in this transition pressure case when the global pressure is not far away enough from the saturation pressure, due to local rapid mixing or heat transfer processes, some parts of the plume may evaporated or broke up faster and entered the flash boiling scheme at a microscopic level.

While SMD is a straightforward metric to compare the overall droplet sizes among different test points, it should be noted that the measurement region was fixed in location, but the spray plume was in motion and in the meantime droplets within the plume were encountering breakup and evaporation processes. Hence, such a single number metric may not be able to fully represent these complex physical phenomena. Therefore, it is worth checking individual droplet size distributions against the actual image of the spray plume to better understand the effect of ambient pressures on the droplet sizes. Figures 10 – 12 show the spray image obtained from backlit imaging (images in the left column) and its corresponding volumetric droplet size distribution measured by Spraytec (histograms in the right column) at some given timings of interest for the 13 bar (Figure 10), the 8 bar (Figure 11), and the 5 bar (Figure 12) test points, respectively. Note that in the histograms the droplet sizes are reported in a log scale, and the edges of the bins were preset to match with the optimal measurement ranges for the photodiode detectors within the Spraytec receiver [28].

Two immediate observations can be made from these figures. First, due to the plume motion, the droplet sizes were indeed measured in different parts of the plume at the reported timings. At 1.2 ms aSOI, the front edge of the plume entered the measurement region (bounded by the red dashed lines in the images) and its droplet sizes were measured and reported in the histograms, while at later timings (after 1.4 ms aSOI), the necking part of the plume was measured. Another observation reveals a finding which was hidden by the single number metric of SMD — each of the histograms of the droplet sizes followed a bi-modal distribution whose two peaks are respectively at around 12 µm and 120 µm, and there were almost no droplets fell in the bins at around 30 µm. To promote later discussions, a cut-off threshold was selected at 34.1 µm (at the edge of a bin in the histogram), and the cumulated volumetric frequencies below and above the threshold were reported by the two numbers (in a purple font color) in each histogram. These numbers therefore showed the cumulative volumetric frequency for the respective parts of the bi-modal distribution, each of which further corresponds to the smaller (left part of the histogram) and larger (right part) droplets within the plume.

For non-flash boiling cases as exemplified by the 13 bar chamber pressure case in Figure 10, the droplet size distribution was almost unaltered at the front edge (at 1.2 ms aSOI, Figure 10(a)) and at the necking part

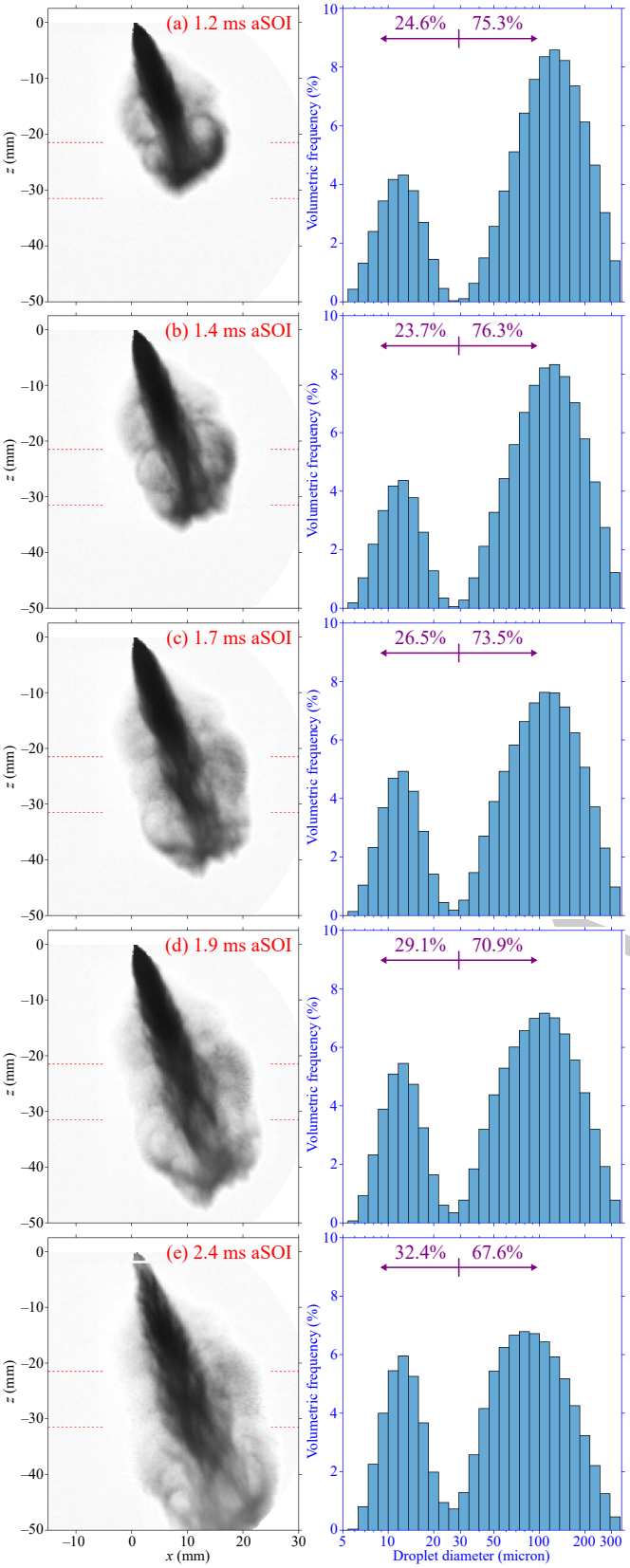

Figure 10: Ammonia spray images (left column) and histograms of droplet size distributions (right column) simultaneously measured in the region between the red dashed lines at different timings (rows) and 13 bar chamber pressure.

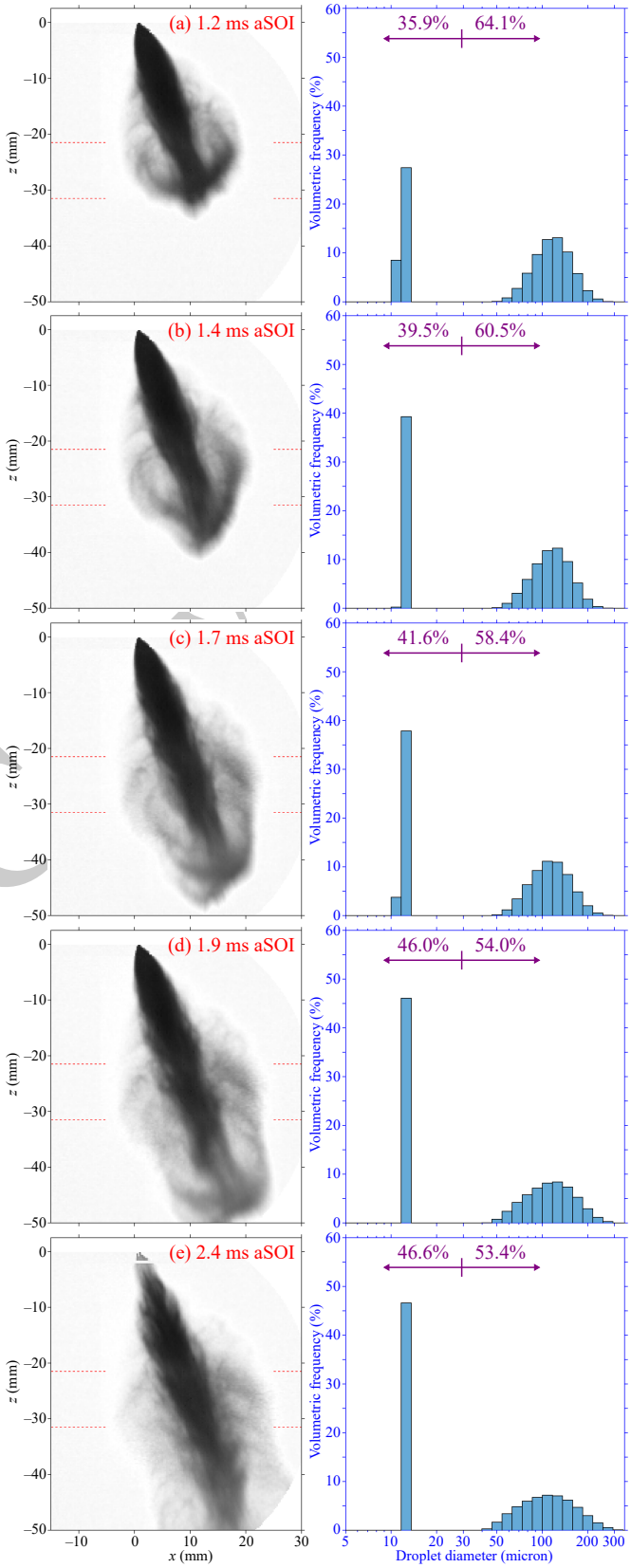

Figure 11: Ammonia spray images (left column) and histograms of droplet size distributions (right column) simultaneously measured in the region between the red dashed lines at different timings (rows) and 8 bar chamber pressure.

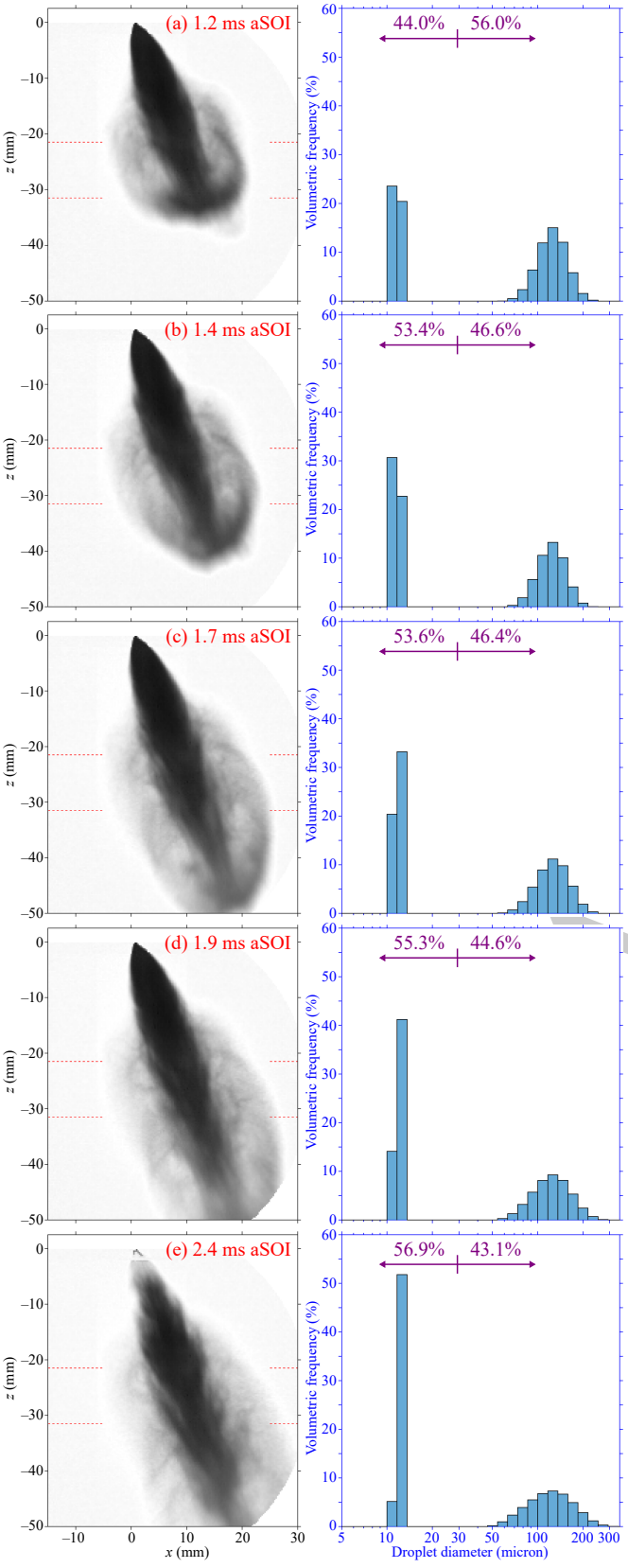

Figure 12: Ammonia spray images (left column) and histograms of droplet size distributions (right column) simultaneously measured in the region between the red dashed lines at different timings (rows) for 5 bar chamber pressure.

(at 1.4 ms aSOI, Figure 10(b)) of the plume, and the majority (over 75%) of the droplet volumes were concentrated in the larger droplets (right part of the histogram). At later timings, as larger droplets gradually evaporated and broke into smaller ones, the volume occupied by the larger droplets reduced to 73.5% at 1.7 ms aSOI (Figure 10(c)), then to 70.9% at 1.9 ms aSOI (Figure 10(d)), and finally to 67.6% at 2.4 ms aSOI (Figure 10(e)). Also, in the larger droplet partition (right partition of each histogram), the highest peak shifted towards smaller values from the 116.6 – 135.9 µm bin (Figure 10(a) and (b)) to the neighboring bin (100 – 116.6 µm, Figure 10(c) and (d)) and finally to the next one (85.8 – 100 µm, Figure 10(e)), indicating that the larger droplets disappeared faster than the smaller ones. Meanwhile, the cumulative volume frequency for the smaller droplets (left partition of each histogram) slowly increased. Despite the valley near the cut-off threshold (again at 34.1 µm), each partition of the bi-modal distribution showed a relatively flat and a somewhat normal distribution — none of the bins exceeded 9% in terms of the volumetric frequency.

The front part for the plumes under flash-boiling cases such as the 5 bar chamber pressure case in Figure 12(a), on the other hand, had a much smaller portion occupied by larger droplets (56.0% by volume at 1.2 ms aSOI) compared to the higher pressure case (75.3% by volume at 1.2 ms aSOI in Figure 10(a)), owing to its rapid evaporation and breakup processes. Also, this portion of larger droplets dropped drastically when compared to the rear part of the plume entered the measurement region only 0.2 ms afterwards at 1.4 ms aSOI at this test point (46.6% by volume in Figure 12(b)). After this sudden shift towards the smaller droplets, within the next 1 ms, while the larger droplets were breaking into smaller ones, the cumulated volumetric frequency showed a gradual decrease on the larger droplet side (from 46.6% at 1.4 ms aSOI in Figure 12(b) to 43.1% at 2.4 ms aSOI in Figure 12(e)), and this partition of the bi-modal distribution became flatter at later timings without any shift on its highest peak (consistently located at 116.6 – 135.9 µm). After converting the volume-based frequency (Figure 12) to the number-based one (figure not shown for brevity), it was confirmed that there were more droplets ranging from 116.6 – 135.9 µm (the highest peak) than the bin to the right of it (from 135.9 – 158.5 µm), and when these droplets in both bin categories underwent the breakup process, there were more droplets broke up in the former bin than the latter, causing the distribution appeared to be flatter. Meanwhile, a corresponding increase of the cumulated volume frequency occurred on the smaller droplet partition of these histograms. A deeper look into the distribution of the smaller droplet partition, however, showed an unusual phenomenon — unlike the non-flash boiling case in Figure 10, the sizes of the smaller droplets in the flash boiling case in Figure 12 concentrated in a narrow range (from 10.0 – 13.6 µm), and at later timings such as Figure 12(d) and (e), there were over 40% by volume of droplets have a diameter between 11.7 – 13.6 µm (the high spike in Figure 12(d) and (e)).

The transition region near the global saturation pressure, for instance at 8 bar in Figure 11, showed a mixed behavior of both non-flash boiling and flash-boiling cases. On the larger droplet partition, the peak of the distribution shifted towards the smaller side similar to the non-flash boiling case in Figure 10, and the distribution also flattened following the pattern observed in the flash-boiling case in Figure 12. Also, the smaller droplet partition of the distributions in Figure 11 had a spike between 11.7 – 13.6 µm, which was a phenomenon observed in the flash-boiling case in Figure 12.

Owing to a stronger evaporation and more breakup occurred under the flash boiling cases, the portion of the smaller droplets in the plume necking part increased as the ambient pressure decreases – from 23.7% (by volume) at 13 bar in Figure 10(b), to 39.5% at 8 bar in Figure 11(b) and 53.4% at 5 bar in Figure 12(b). Correspondingly, the portion of the larger droplets decreased under lower ambient pressure conditions.

It is worth noting that the bi-modal distribution for droplet sizes shown in Figures 10 – 12 and the high spike between 10.0 – 13.6 µm observed in Figure 11 and Figure 12 are not commonly reported in literature. The cause of such phenomena is still under investigation. It was found that one of the detectors in the Spraytec device showed a higher signal compared to its neighboring channels, which may be a "real" result or an instrumentation error. If it is a "real" result, as a hypothesis waiting to be proven, each of the two modes in Figures 10 – 12 could have resulted from the larger droplets in the plume body (a bulk of darker pixels in the images) and the smaller ones in the mist around (outside of the plume body), respectively. Meanwhile, when a larger "parent" droplet breaks up due to internal cavitation under strong flash boiling cases (such as in Figure 11 and Figure 12), its volume may be almost equally distributed into the resulting "child" droplets. There exists, therefore, a favored volume (and hence diameter) of the child droplets because of this process, causing the observed high spike. On the other hand, if it is an instrumentation error, due to the methodology employed by the Spraytec software, such a signal (which would be a systematic error for all the test points if it is an instrumentation error) may also exaggerate the high spike and suppress the neighboring size bins. These hypotheses will be investigated by more experiments in future work.

Conclusion

Liquid anhydrous ammonia at 150 bar was sprayed from a GDI injector into a constant volume chamber at various chamber pressures and at a fixed duration of 2 ms, to examine the effect of ambient pressure on the macroscopic and microscopic characteristics of ammonia sprays at room temperature. The optical access of the chamber enabled a backlit imaging technique for spray morphology studies and a laser diffraction technique for droplet size measurements to be implemented at the same time. The ambient pressure conditions spanned the flash-boiling region (lower pressure), the non-flash boiling region (high pressure) and the transition region (medium pressure) of ammonia, and the small increment (1 bar) between the neighboring test points allowed a detailed investigation on the trend of ammonia sprays across the saturation vapor pressure of ammonia (8.5 bar at 20 °C [6, 7]). The macroscopic parameters, including the maximum penetration lengths, spray centerline angles and spread widths, were computed from the backlit images recorded at 10 kFPS using the SAE J2715 standard [21, 22]. For each image, the microscopic droplet size distribution within the plume was also measured simultaneously, and the Sauter mean diameter was computed as well. A summary of the key findings is provided in the following paragraphs.

Ambient pressure has a profound effect on the geometry of ammonia spray plumes. Due to a larger resistance caused by a higher density, at a given time after the start of injection, the maximum penetration length of the spray plume monotonically reduced as the the ambient pressure increased. When evaluated at a fixed length away from the injector tip, the spray spread width was also smaller when the ambient pressure was higher. Numerically speaking, the penetration length and the spread width reduced by about 10 mm (over 22% at 1.4 ms aSOI) and 2.5 mm (over 31% at 15 mm away from the injector tip), respectively, from the values at 5 bar ambient pressure compared to the values at 13 bar. The transition from the flash-boiling region to the non-flash boiling region appeared to be gradual in terms of the macroscopic parameters.

On a side note, changing the working fluid to liquid ammonia does not alter the designed spray centerline angle for this GDI injector. The spray centerline angles showed a small variation at different ambient pressures and timings, and the averaged value was close to the designed value.

The droplet sizes measured within the plume, on the other hand, showed a more abrupt change near the saturation pressure of ammonia. While generally the SMD values increased as the chamber pressure became higher, in the flash-boiling region and for test points near the saturation pressure (3 – 9 bar), the SMD values increased drastically from about 16 µm at 3 bar to 24 µm at 9 bar, indicated that the droplet breakup process depends strongly on the variation of ambient pressure under these conditions. Once the chamber pressure was high enough and entered the non-flash boiling region (above 9 bar), changing ambient pressures have a minimal effect on the SMD values. The droplet sizes, when quantified by a size distribution chart, showed a bi-modal distribution in all cases. At higher chamber pressures, each partition of the distribution was somewhat Gaussian, and the volumetric frequency for the smaller diameter part gradually increased as larger droplets evaporated at a later timing. In contrast, in the flash boiling region, it was observed that there existed a favorable diameter (at around 12 µm) for the child droplets when the larger parent droplets broke up, and this led to a spike on the histogram for the lower ambient pressure test points. Such a phenomenon was not found when the ambient pressure was higher, and its exact cause will be investigated by future experiments.

This set of test provides a fundamental dataset for future model validation. As part of the future work, more tests will be conducted to generate a more comprehensive collection of ammonia spray datasets under various conditions. These datasets will also provide an opportunity to further investigate the cause of the bi-modal droplet size distribution observed in the current measurement, and help validate the hypothesis of the favorable child droplet size during the droplet breakup process discussed in the previous section.

List of Abbreviations

aSOI	After the start of injection
DI	Direct injection
FOV	Field of view
FPS	Frames per second
GDI	Gasoline direct injection
GHG	Greenhouse gas
LED	Light-emitting diode
PDA	Phase doppler anemometry
PDIA	Particle droplet image analysis
SMD	Sauter mean diameter
TTL	Transistor-to-transistor logic
XCT	X-ray computed tomography

References

[1] International Energy Agency, "Net Zero by 2050," (Paris, 2021).

[2] "Reducing emissions from the shipping sector," European Commission, 2023, Available at: https://climate.ec.europa.eu/eu-action/transport/reducing-emissions-shipping-sector_en, accessed: Oct. 2023.

[3] "Production capacity of ammonia worldwide from 2018 to 2021," GlobalData, 2022, Available at: https://www.statista.com/statistics/1065865/ammonia-production-capacity-globally/, accessed: Oct. 2023.

[4] Ley, C. and Elvers, B., eds., "Ullmann's Encyclopedia of Industrial Chemistry," 7th ed., (Weinheim, Wiley-VCH, 2011), ISBN:978-3-527-32943-4.

[5] The Royal Society, "Ammonia: zero-carbon fertiliser, fuel and energy store," Policy briefing, (London, The Royal Society, 2020), ISBN:978-1-78252-448-9.

[6] "NIST Chemistry WebBook," NIST Standard Reference Database Number 69, The National Institute of Standards and Technology, 2023, doi:10.18434/T4D303, accessed: Oct. 2023.

[7] Stull, D. R., "Vapor Pressure of Pure Substances. Organic and Inorganic Compounds," *Industrial & Engineering Chemistry* 39(4): 517–540, 1947, doi:10.1021/ie50448a022.

[8] Van Itterbeek, A., Verbeke, O., Theewes, F., Staes, K., et al., "The difference in vapour pressure between normal and equilibrium hydrogen. Vapour pressure of normal hydrogen between 20K and 32K," *Physica* 30(6): 1238–1244, 1964, doi:10.1016/0031-8914(64)90114-4.

[9] Valera-Medina, A., Xiao, H., Owen-Jones, M., David, W. I., et al., "Ammonia for power," *Progress in Energy and Combustion Science* 69: 63–102, 2018, doi:10.1016/j.pecs.2018.07.001.

[10] Bicer, Y. and Dincer, I., "Life cycle assessment of ammonia utilization in city transportation and power generation," *Journal of Cleaner Production* 170: 1594–1601, 2018, doi:10.1016/j.jclepro.2017.09.243.

[11] Mounaïm-Rousselle, C. and Brequigny, P., "Ammonia as Fuel for Low-Carbon Spark-Ignition Engines of Tomorrow's Passenger Cars," *Frontiers in Mechanical Engineering* 6: 70, 2020, doi:10.3389/fmech.2020.00070.

[12] Senecal, K. and Leach, F., "Racing Toward Zero: The Untold Story of Driving Green," (Warrendale, PA, SAE International, 2021), ISBN:978-1-4686-0146-6.

[13] Stone, R., "Introduction to Internal Combustion Engines," 4th ed., (London, Red Globe Press, 2012), ISBN:978-0-230-57663-6.

[14] Leach, F., Ismail, R., and Davy, M., "Engine-out emissions from a modern high speed diesel engine – The importance of Nozzle Tip Protrusion," *Applied Energy* 226: 340–352, 2018, doi:https://doi.org/10.1016/j.apenergy.2018.05.117.

[15] Zhang, Z., Li, T., Chen, R., Wang, N., et al., "Injection characteristics and fuel-air mixing process of ammonia jets in a constant volume vessel," *Fuel* 304: 121408, 2021, doi:10.1016/j.fuel.2021.121408.

[16] Pelé, R., Mounaïm-Rousselle, C., Bréquigny, P., Hespel, C., et al., "First Study on Ammonia Spray Characteristics with a Current GDI Engine Injector," *Fuels* 2(3): 253–271, 2021, doi:10.3390/fuels2030015.

[17] Cheng, Q., Ojanen, K., Diao, Y., Kaario, O., et al., "Dynamics of the Ammonia Spray Using High-Speed Schlieren Imaging," *SAE International Journal of Advances and Current Practices in Mobility* 4(4): 1138–1153, 2022, doi:10.4271/2022-01-0053.

[18] Fang, Y., Ma, X., Zhang, Y., Li, Y., et al., "Experimental Investigation of High-Pressure Liquid Ammonia Injection under Non-Flash Boiling and Flash Boiling Conditions," *Energies* 16(6): 2843, 2023, doi:10.3390/en16062843.

[19] Li, X., Wang, S., Yang, S., Qiu, S., et al., "A review on the recent advances of flash boiling atomization and combustion applications," *Progress in Energy and Combustion Science* 100: 101119, 2024, doi:10.1016/j.pecs.2023.101119.

[20] Liu, X., Yao, X., Wang, Z., and Tang, C., "Single hole ammonia spray macroscopic and microscopic characteristics at flare and transition flash boiling regions," *Applied Thermal Engineering* 235: 121443, 2023, doi:10.1016/j.applthermaleng.2023.121443.

[21] SAE Gasoline Fuel Injection Standards Committee, "Gasoline Fuel Injector Spray Measurement and Characterization," SAE Standard J2715, 2007, doi:10.4271/J2715_200703.

[22] Hung, D. L., Harrington, D. L., Gandhi, A. H., Markle, L. E., et al., "Gasoline fuel injector spray measurement and characterization – A new SAE J2715 recommended practice," *SAE International Journal of Fuels and Lubricants* 1(1): 534–548, 2009, doi:10.4271/2008-01-1068.

[23] Shen, L. and Leach, F., "An introduction to ammonia spray lab safety and setup," Presented at the Second Symposium on Ammonia Energy, July 2023, Available at: https://safety.admin.ox.ac.uk/safety-in-action#collapse4367526, accessed: Oct. 2023.

[24] "Code of Practice 18," version 3, The British Compressed Gases Association, 2014, Available at: https://bcga.co.uk/publications/cp18-the-safe-storage-handling-and-use-of-special-gases-revision-3-2014/, accessed: Oct. 2023.

[25] "Code of Practice 35," version 3, The British Compressed Gases Association, 2022, Available at: https://bcga.co.uk/publications/cp35-filling-ratios-and-developed-pressures-for-liquefied-and-compressed-gases/, accessed: Oct. 2023.

[26] Health and Safety Executive, "EH40/2005 Workplace exposure limits," 4th ed., (Norwich, TSO (The Stationery Office), 2020), ISBN:978-0-7176-6733-8.

[27] "Ammonia Incident Management," PHE publications gateway number: 2014790, Public Health England, 2019, Available at: https://assets.publishing.service.gov.uk/government/uploads/system/uploads/attachment_data/file/825191/Ammonia_IM_PHE_140819__1_.pdf, accessed: Oct. 2023.

[28] "Spraytec User Manual," Malvern Instruments Ltd., (Worcestershire, 2007).

[29] Sauter, J., "Die Grössenbestimmung der im Gemischnebel von Verbrennungskraftmaschinen vorhandenen Brennstoffteilchen," [The determination of the size of the fuel particles present in the mixture mist of internal combustion engines] (in German), (VDI-Verlag (VDI publishing house), 1926).

[30] Pacek, A. W., Man, C. C., and Nienow, A. W., "On the Sauter mean diameter and size distributions in turbulent liquid/liquid dispersions in a stirred vessel," *Chemical Engineering Science* 53(11): 2005–2011, 1998, doi:10.1016/S0009-2509(98)00068-2.

[31] Kowalczuk, P. B. and Drzymala, J., "Physical meaning of the Sauter mean diameter of spherical particulate matter," *Particulate Science and Technology* 34(6): 645–647, 2016, doi:10.1080/02726351.2015.1099582.

[32] Mayinger, F. and Feldmann, O., eds., "Optical Measurements, Techniques and Applications," 2nd ed., (Berlin, Springer, 2001), ISBN:978-3-642-63079-8.

[33] Merkus, H. G., "Particle Size Measurements, Fundamentals, Practice, Quality," (Dordrecht, Springer, 2009), ISBN:978-1-4020-9015-8.

[34] Bradley, D. and Roth, G., "Adaptive Thresholding using the Integral Image," *Journal of Graphics Tools* 12(2): 13–21, 2007, doi:10.1080/2151237x.2007.10129236.

Contact Information

For queries, please contact Li Shen (sam-li.shen@eng.ox.ac.uk) and Felix Leach (felix.leach@eng.ox.ac.uk) from the Department of Engineering Science, University of Oxford, OX1 3PJ.

Acknowledgments

This research was funded in whole or in part by Engineering & Physical Sciences Research Council (EPSRC, EP/V04673X/1). For the purpose of Open Access, the authors have applied a CC BY public copyright license to any Author Accepted Manuscript (AAM) version arising from this submission. The authors would also like to thank Prof. Richard Stone FREng, Prof. Ben Williams and Mr. Philip Paling from our department for their help when building the test facilities, as well as Prof. David L.S. Hung from Shanghai Jiao Tong University and three anonymous reviewers for their valuable comments. Data supporting this paper is available from the "Oxford Research Archive" repository at https://ora.ox.ac.uk/.